Highlights

Surface state of NiOOH under oxidative conditions: Can dopants induce surface oxidation?

Laureline Treps, Tony Ermacora, Andrea Giacomelli, Carine Michel, Stephan N. Steinmann

- The stoichiometric (50%) hydrogen coverage on the NiOOH surface under electro-oxidation conditions (around 1.5 V vs RHE) is most stable

- Doping of NiOOH and $Ni(OH)_2$ is generally slightly endergonic

- Substitutional doping of NiOOH with V, Cr, Mn and Fe reduces the bulk redox potential

- Cr doping leads to an exceptional Ni(III) stabilisation at the surface

Surface state of NiOOH under oxidative conditions: Can dopants induce surface oxidation?[*]

Laureline Treps[a], Tony Ermacora[a], Andrea Giacomelli, Carine Michel and Stephan N. Steinmann

CNRS, ENS de Lyon, LCH, UMR 5182, , Lyon cedex 07, 69342, , France

ARTICLE INFO

Abstract

Nickel oxyhydroxide (NiOOH), featuring redox-active Ni[III], is a one of the best non-noble electro-oxidation catalyst in alkaline solution. However, NiOOH is only stable at potentials ≥ 1.5 V vs RHE, with Ni(OH)$_2$ being the stable reduced form at lower potentials. The potential of the phase transition from inactive Ni(OH)$_2$ to active NiOOH can be tuned by doping. Lowering the potential for reaching the phase-transition is thought to be beneficial for lowering the overpotential of oxidation reactions catalysed by NiOOH. Here, we investigate which first row transition metals are most plausible for this purpose: First, the doped structure should be more stable than the phase-segregated system and second the potential for reaching the NiOOH-like phase should be lower compared to the pure Ni compound. Substitutional doping of NiOOH is found to be plausible for many dopants, but only V can be incorporated exothermically compared to their pure oxyhydroxides. Furthermore, dopants lead to a substantial lowering in the potential necessary to reach the phase transition. Since catalysis is more a surface than a bulk process, we then investigate the surface state of NiOOH and the impact of substitutional doping on it. To address this question, we apply grand-canonical density functional theory (GC-DFT) in order to explicitly account for the electrochemical potential. We find that the stoichiometric surface (50% hydrogen coverage) is the most stable one over a large range of relevant potentials at pH 14. Oxidizing the surface lowers the hydrogen coverage and occurs at about 1.7 V vs RHE, i.e., $\sim$0.2 V less positive compared to the potential of the phase transition. At a doping level of 25%, only V and Cr allow to stabilize Ni[III] at significantly lower potentials compared to pure NiOOH (down to 1.1 V vs RHE) in the bulk. Furthermore, vanadium, chromium and manganese might be suitable choices as these metal centers, which remain in the +III or +IV state at lower potentials compared to Ni, could also act as active sites in electro-oxidation reactions.

1. Introduction

In light of pressing environmental issues such as pollution and the greenhouse effect, there is a necessity to search for clean energy sources. This has led to the exploration of alternatives to fossil fuel-derived energy, such as biomass-derived energy and green hydrogen production as an energy vector. Consequently, the global shift towards renewable energy requires innovative solutions for efficient energy storage and conversion, prompting increased development of electric devices for this purpose. These devices rely on efficient catalytic materials at the electrodes to produce or convert fuels. [1]

Hydrogen production through alkaline water electrolysis involves the splitting of water using an electric current in a basic medium, where the hydrogen evolution reaction (HER) occurs at the cathode and the oxygen evolution reaction (OER) at the anode. However, the OER remains responsible for the major part of the electricity cost of water electrolysis, mainly because of thermodynamics in combination with significant overpotentials and sluggish kinetics. [2]

Various catalysts have been proposed over the past few decades to enhance the efficiency of the OER. While some noble metal-based catalysts have shown promising results in terms of efficiency and low energy consumption, their widespread use is limited by economic factors together with their intrinsic rarity in the Earth crust. [3, 4] Recently, materials based on metal hydroxides have been considered for the OER. Several studies have highlighted the efficiency of nickel oxyhydroxide (NiOOH) as an active anode catalyst for water and biomass electrolyzers under alkaline conditions, especially for catalyzing the OER reaction. [2, 5–11] Co-electrocatalysis, which replaces the OER with the oxidation of organic molecules, has been investigated as a means to enhance hydrogen production efficiency. For example, reactions involving organic molecules such as biomass-derived alcohols, 5-hydroxymethylfurfural (HMF), and natural plant derivatives have shown promise, leading to greater energy efficiency in hydrogen production. [12]

NiOOH primarily exists in four different phases, with β-NiOOH identified as the most active for catalytic activities. [5, 13, 14] The crystalline structure of β-NiOOH is not fully understood but is generally described as NiOOH layers bonded by hydrogen bonds. [15–17] Experimental and theoretical studies suggest that hydrogen atoms are randomly distributed between the nickel layers. [16, 18]

In the mechanism proposed by Fleischmann *et al.* [19, 20], the Ni[III]/Ni[II] transition is thought to be key in the electrochemical behavior of nickel-based oxides during so called "indirect" oxidation reactions. In these reactions, the electron is transferred to Ni[III], instead of being directly injected in the electrical circuit. In other words, Ni[III] acts

---

as a chemical oxidant that is then regenerated by the electrochemical potential. An alternative mechanism is the so called "potential-dependent" oxidation, where the active species is supposed to be metastable Ni^{IV} sites whose generation is rate-determining and which do not remain stable at open-circuit potential. Experimental studies suggest that (aromatic) aldehydes primarily react through the Fleischmann mechanism, whereas alcohols primarily react via a potential-dependent oxidation.[21]

The major drawback of NiOOH is the high potential ($\sim$ 1.5 V vs RHE) needed to form it, with Ni^{II}, mostly in the form of $Ni(OH)_2$, being the resting state at lower potentials. A major hypothesis in the literature is that if one would be able to reach the NiOOH-phase at lower potentials, the corresponding material should still contain Ni^{III} and, thus, still be active for oxidation reactions.[22] If this was the case, the energy requirement for the oxidation reaction could proportionally be reduced. Several studies have demonstrated the effectiveness of different dopants in modulating the electrochemical properties of NiOOH. First, non-metal dopants or their precursors such as phosphorus,[23] fluorine[24] and sulfur[25] have been explored to tailor the electronic properties of NiOOH. However, these elements are generally replaced by oxygen under the operating oxidizing alkaline conditions, so that their influence is more related to the morphology of the resulting catalyst than to intrinsic properties induced by the dopants.[26] The second kind of doping involves the metal centers. In particular, the incorporation of iron (Fe) has been shown to reduce the overpotential for water oxidation, enhancing the catalytic efficiency of NiOOH-based cathodes.[27, 28] Other dopants have also been explored with varying success and limited understanding.[22, 26] On the one hand the dopant itself can act as an active site. On the other hand, metal incorporation alters the electronic structure and local environment of the nickel centers, potentially increasing the availability of Ni^{III}. The investigation of this hypothesis is the major topic of this work.

Theoretical models are employed to complement experimental results and guide development of relevant solutions. Density Functional Theory (DFT) is widely recognized for its effectiveness in modeling catalytic properties.[29–31] The reliability of the DFT+U formalism has been determined for NiOOH through comparison to both theoretical and experimental benchmark data.[30, 32, 33] These studies concluded that PBE+U provides the best balance between computational time and accuracy. Regarding the treatment of the electrochemical potential, the best compromise between computational effort and captured effects is currently reached at the level of grand-canonical DFT (GC-DFT) in combination with an implicit solvent.[34] This approach has been used in diverse contexts, including the screening of dopants.[35]

One of the challenges for studying NiOOH computationally is that the bulk structure of NiOOH is not unambiguously identified. While it is well accepted that it is a layered compound, derived from the layered $Ni(OH)_2$,

the protons seem to be quite disordered and mobile in experiments. [18] Therefore, we start our study by investigating several proton arrangements to identify the most suitable one for the continuation of the study. Then, we determine the surface state, i.e., the hydrogen coverage, under applied potentials using grand canonical DFT+U. This approach has been found suitable in previous work on CoOOH, a related material.[36] Then, we systematically investigate the impact of substitutional doping with all first row transition metals (Sc, Ti, V, Cr, Mn, Fe, Co, Cu, and Zn) on the oxidation potential and, for the most relevant ones, we have determined the potential-dependent surface states. Only few dopants have a significant effect on the potential of the phase-transition and allow to stabilize Ni^{III} at 0.2 V lower potentials compared to pure NiOOH. Therefore, our study guides the rational selection of substitutional dopants in NiOOH for lowering the energy demand in alkaline water or biomass electrolysers.

2. Method and calculation details

2.1. Method

The computational hydrogen electrode (CHE) model is used for electrochemical thermodynamics. [6] Accordingly, the standard Gibbs free energy of a proton–electron couple is defined by replacing the combined energy of ($H^+ + e^-$) with half the free energy of H_2 in the gas phase at 0 V vs RHE:

$$\mu_{H^+} + \mu_{e^-} = \frac{1}{2} G_{H_2} \qquad (1)$$

Under standard conditions (pH = 0, T = 298 K, P = 1 bar) the reaction free energy ΔG is expressed as :

$$\Delta G_x(U) = \Delta G_x + n(\mu_{H^+} + \mu_{e^-} - eU) \qquad (2)$$

ΔG_x represents the free energy of the reaction involved, determined through DFT calculations, including electronic energy (E), entropy (S), a zero-point energy correction (ZPE) and an enthalpic correction ($\Delta H_{0 \to T}$) : $G = E + ZPE + \Delta H_{0 \to T} - TS$. Additionally, a term neU is introduced when the potential differ from 0 V versus RHE. This includes the number of protons coupled to electrons transferred in the reaction (n>0 for an oxidation and n<0 for a reduction), the elementary charge (e), and the electrode potential (U).

Since proton activity depends on the pH of the solution, adjustments are required in electrochemical settings, where pH and voltage vary. The relationship between the pH of the system and the potential U is determined by the following equation :

$$U_{RHE} = U_{SHE} + k_B T \cdot pH \ln(10) \qquad (3)$$

The grand canonical DFT (GC-DFT) method is used to model the electrochemical electrode potential. GC-DFT

explicitly accounts for variations of the surface charge, allowing for the potential to influence reaction kinetics and thermodynamics. This capability enables accurate modeling of systems under varying potentials. The electrode potential is determined using the Fermi-level, i.e., the chemical potential of electrons. [37–41] Its free energy (G) is computed as a function of the electrochemical potential (U):

$$G(U) = E(U) - q_{\text{surf}}(U) \cdot U \approx E(U_0) - \frac{1}{2}C \cdot (U - U_0)^2 \quad (4)$$

$E(U)$ is the corresponding electronic energy at a potential U. q_{surf} is the surface charge, positive when electrons are removed and negative when electrons are added. U_0 is the work function of the system at zero charge, and $E(U_0)$ is the energy used in the CHE framework. The second equivalence holds for metallic (gap-less) systems, where the grand canonical energy $G(U)$ can be expanded to the second order in terms of the capacitance C of the system. A quadratic fit to DFT data for at least 4 different charge states then allows to describe the system's energy analytically as a function of the electrochemical potential.

2.2. Computational Details

All computations were done via the *Vienna Ab initio* Simulation Package (VASP) [42] based on periodic spin-polarized density functional theory (DFT), using the projector-augmented-wave (PAW) [43] formalism to represent the core-valence electron interaction. The Perdew-Burke-Ernzerhof (PBE) [44] exchange-correlation functional was used, supplemented by the dDsC dispersion correction [45] to account for van der Waals (vdW) interactions.

Convergence tests were performed to select the plane-wave cutoff energy and k-point mesh size. As a result, the cutoff energy of 500 eV was chosen. A Monkhorst-Pack mesh of $3 \times 3 \times 2$ k-point grid was employed for $2 \times 2 \times 2$ cell bulk calculations. The k-point mesh was accordingly scaled with the size of the supercell. H_2 was computed within a cubic box of 10 Å. The energy convergence criterion for the self-consistent-field (SCF) cycles was set to 10^{-6} eV per cell. The Hubbard correction was set to a U-J value of 5.5 eV on Nickel 3d orbitals. [46] A Fermi smearing of 0.025 eV (290 K) has been applied.

We used $2 \times 2 \times 2$ unit cells for the pure nickel bulk study and a $2 \times 4 \times 2$ unit cell for the doped bulk study, resulting in a total of 16 nickel atoms with doping concentrations ranging from 6.25% (1 dopant) to 25.0% (4 dopants). The NiOOH slab was modeled using a 2×4 supercell. A symmetrization process was applied resulting in a four-layered slab to avoid surface dipole moments and obtain unambiguous workfunctions.

To account for solvation effects, we used the implicit solvation model as implemented in VASPsol. The model is based on the linearized Poisson-Boltzmann (PB) equation, integrates an idealized electrolyte distribution into electronic structure calculations, and neutralizes surface charge imbalances. [47]

Harmonic vibrational and thermal corrections to the Gibbs energy at 300 K have been determined using VASP-KIT package,[48] where H_2 is treated as an ideal gas in the rigid rotor approximation.

The Ni oxidation states of individual metal atoms were identified based on the magnetic moments as obtained from the site-projection scheme implemented in VASP. The Ni^{II}, Ni^{III}, and Ni^{IV} sites have magnetic moments of 1.7, 1.1, and 0, respectively.

3. Results and discussion

We first present a detailed analysis of bulk pure and doped NiOOH. Expanding on previous structural studies [49, 50] we explore a broader range of hydrogen atom distributions and identify the most stable NiOOH bulk. We also examined the effects of substitutional doping with first-row transition metals on the oxidation potential, specifically the transition from Ni^{II} to Ni^{III}. Subsequently, we explored the relevant surface state, focusing on the hydrogen coverage at varying applied potentials and pH values. Finally, we analyzed the oxidation states of Ni centers, with particular focus on how dopants modify the surface oxidation potential and the associated electronic structure. This provided insights into the electrochemical behavior of substitutional doping effects on NiOOH.

3.1. NiOOH bulk

We begin our analysis with several bulk β-NiOOH structures derived from the literature, including triclinic and monoclinic geometries. Figure 2 shows the H distribution tested in NiOOH bulk with a focus on the positioning of protons in different configurations. Table S1 lists the lattice parameters and relative energies for each configuration. The structure labeled **A** is based on the work of Eslamibidgoli *et al.* [49]. Structures **B** and **C** are modifications of structure **A**, with different proton positions to allow for a more comprehensive exploration of proton configuration. Structures **D** and **E** are derived from the study by Zaffran and Toroker [50].

Structure **A** features protons aligned along $\vec{a}$ and staggered along $\vec{b}$, while structures **B** and **C** feature staggered arrangements along $\vec{a}$ and $\vec{b}$. **B** has the two layers identical, whereas **C** is alternating hydrogen distribution between the two layers. Structure **D** has protons aligned along both $\vec{a}$ and $\vec{b}$. Structure **E** consists of an alternating arrangement of NiO_2 and $Ni(OH)_2$ layers. All structures describe the oxidation states of the nickel atoms according to expectations, except for structure **E**. In structure **E**, the nickel atoms within the $Ni(OH)_2$ layers are identified as Ni^{II}, while the nickel atoms within the NiO_2 layers are identified as having an equal ratio of Ni^{III} and Ni^{IV} character, indicating questionable electron delocalisation.

Regarding the stability, the relative Gibbs free energy (G_{rel}) reveals minimal variations among the tested configurations. Structure **E** is the most stable configuration found. The energy difference between structures **A** and
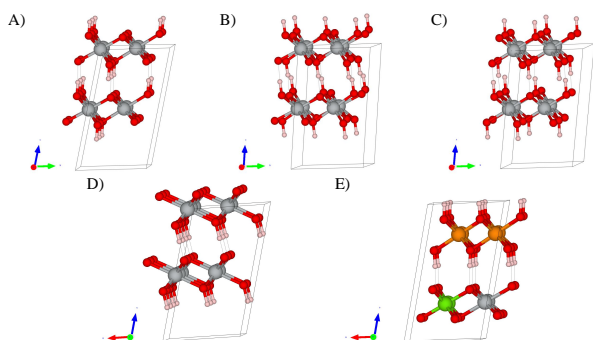
Figure 1: Bulk unit cells used to test effect of positioning protons in β-NiOOH(0001). (A, B, C) Triclinic structure from ref 49. (D, E) Monoclinic structures from ref 50. The Ni^{II}, Ni^{III} and Ni^{IV} atoms are displayed in orange, gray and green, respectively. The vectors a, b and c are shown in red, green and blue, respectively.
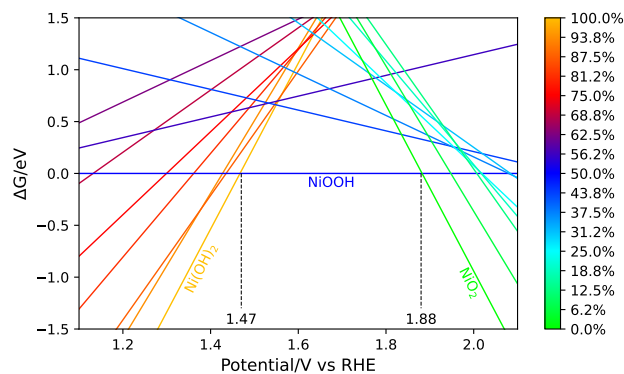

Figure 2: Relative stability of nickel bulk oxidation states as a function of electrochemical potential (corresponding to Eq. 5). The color bar represents the hydrogenation of the bulk, ranging from Ni^{II}(OH)$_2$ (100% in orange) to Ni^{III}OOH (50% in blue) and to Ni^{IV}O$_2$ (0% in green).

E is small (0.026 eV), and structure **B** also has a minor difference (0.084 eV), making them relatively comparable in stability. Structures **C** and **D**, however, have a significantly higher energy difference ($\sim$0.24 eV) compared to the others, indicating they are the least stable ones. We note in passing that the NiOOH bulk has a low band gap (0-0.3 eV at our level of theory, as shown in Section S1), suggesting metallic conductivity, which compares with an experimental value of at most 1.7 eV [51] for highly crystalline NiOOH, but mimics well the defect states present in experimental conditions.[52] The contrasts with Ni(OH)$_2$ bulk which exhibits a relatively large band gap at our level of theory (3.45 eV), in line with the characteristics of an insulator reported experimentally.[52] In other words, at sufficiently high electrode potentials the oxidation states changes and the conductivity of the oxide adopts the behavior of metallic conductor. [53]

The results demonstrate that several proton distributions in NiOOH are competitive in relative energy. Structure **E** has the lowest free energy but a symmetric slab, which is required to apply GC-DFT, can not be built with the nominal bulk stoichiometry. Indeed, since the layers are alternating Ni^{IV} and Ni^{II}, a symmetric slab would necessarily have an excess of either Ni^{IV} or Ni^{II}. Therefore, we have chosen the bulk with the lowest electronic energy for the surface models, structure **A**, which allows the construction of a stoichiometric, symmetric NiOOH slab.

Afterwards, we examined the stability of nickel oxidation states in bulk NiOOH, focusing on the oxidation process from Ni(OH)$_2$ (n=-1) to NiO$_2$ (n=+1), see Eq. 5. Given that we are studying bulk processes which have to preserve electroneutrality of the solid, a coupled proton-electron transfer (PCET) occurs.

$$\Delta G(U) = G_{NiO_2H_{1-n}} - G_{NiOOH} + n(\mu_{H^+} + \mu_{e^-} - eU_{RHE})$$

(5)

The oxidation reactions, from Ni(OH)$_2$ to NiOOH and from NiOOH to NiO$_2$, were investigated using the Ni(OH)$_2$

structure from the study by Tkalych et al. [16], as well as structures **A** and **E** from the previous section as starting points, respectively. All possible H distributions were examined to identify the most stable configurations at each oxidation step. The results are shown in Figure 2 as a plot of the Gibbs free energy difference $\Delta G(U)$ as a function of the applied potential, with each line representing a distinct nickel oxide phase. NiOOH was chosen as the reference for the energy plot. A 2×2×2 nickel unit cell was used for these calculations, yielding 16 oxygen atoms with potential sites for hydrogenation. The plot demonstrates a clear transition from Ni^{II}(OH)$_2$ to Ni^{III}OOH at 1.47 V, where the orange and blue lines intersect, and subsequently from Ni^{III}OOH to Ni^{IV}O$_2$ at 1.88 V, where the blue and green lines intersect. The results indicate that only stoichiometric forms of nickel are stable at each potential.

The stability regions for each oxidation state provide insights for optimizing operating conditions in practical applications in electrochemistry. We are particularly interested in the stability domain of NiOOH, as the nickel electrode oxidation to NiOOH was experimentally observed around 1.5 V vs RHE [54], aligning with our theoretical predictions.

The partial Ni^{IV}/Ni^{III} transition (leading to what is called γ-NiOOH) is experimentally typically observed **CM:** around 0.2 V higher than the Ni^{III}/Ni^{II} transformation, concomitant with OER conditions[27]. However, our calculations place the Ni^{IV} transition at 1.9 V vs RHE, a potential at the upper limit reached in typical experiments. This suggests that the bulk model does not accurately represent the electrochemical thermodynamics of nickel in its +IV oxidation state. Indeed, the bulk structure corresponding to the nickel catalyst under OER conditions is often denoted as γ-NiOOH, where the interlayer spacing is expanded through intercalation of alkali-metal cations and a fraction of Ni atoms reach the +IV oxidation state. This phase is, however, beyond the scope of the current investigation

which focuses on the formation of NiOOH at low oxidation potentials.

In summary, our computations identify $\beta-$NiOOH as a material with disordered, probably mobile, hydrogen atom arrangements. It can be reduced to Ni(OH)$_2$ at 1.5 V vs RHE with no partially reduced forms being stable at any potential. At an excessive potential of 1.9 V, NiO$_2$ can be formed, making this phase irrelevant in the context of electrocatalysis in aqueous solutions.

3.2. Doped NiOOH bulk

As described in the previous section, forming NiOOH bulk requires a limiting electrochemical potential of 1.47 V vs RHE at our level of theory. The main objective of substitutional doping is to lower this redox potential, and, thereby, reducing the energy required to activate and use the catalyst. Here, we study the effect of introducing a second metal in the Ni phase by replacing one to four Ni atoms by first row transition metals (Sc to Zn) in a unit cell composed of 16 metal atoms, corresponding to relatively low (6.25%) to moderate doping (25%). In Ni(OH)$_2$, all nickel atoms are equivalent, whereas in NiOOH as described by form **A** of Fig. 1, nickel atoms are either coordinated by two oxygen atoms (O) and four hydroxyl groups (OH), or by four oxygen atoms (O) and two hydroxyl groups (OH). For both compounds, we determine the most stable arrangement of the doping atoms individually. To start, we estimate the stability of the doped structures by computing the mixing energy ΔG_{mix} (Eq. 6), i.e., the energy change of mixing a pure MOOH bulk with NiOOH, where "M" is a first row transition metal.

$$\Delta G_{mix}: \quad yMOOH + xNiOOH \rightarrow (M_y, Ni_x)(OOH)_{x+y} \tag{6}$$
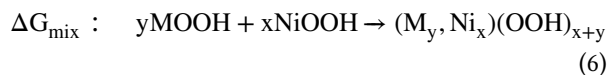
ΔG_{mix} gives information on the possible bulk phase-segregation (if $\Delta G_{mix} > 0$) in the +III state of the material which is assumed to be the active phase of the electrocatalyst. On the contrary, if $\Delta G_{mix} < 0$ the mixing of the two materials is exergonic and, thus, favored. For certain metals, the layered (NiOOH analogue) structure of MOOH is not the most stable polymorph. In that case we use the "staggered" polymorph in which the metal centers are connected in 3D as shown in Fig. S1. This is summarized in Table S2 and shows that for Sc, Ti, V and Cu the layered structure is not the most stable one. Furthermore, bulk ZnOOH is not stable. Therefore, we use bulk Zn(OH)$_2$ instead, as described by Eq. 7.

$$yZn(OH)_2 + xNiOOH \rightarrow (Zn_y, Ni_x)(OOH)_{x+y} + \frac{y}{2}H_2 \tag{7}$$
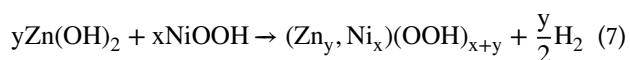
The mixing energy as a function of the doping concentration is depicted in Figure 3a. The higher the mixing energy, the less stable the doped structure, and the less favorable the doping process is. First of all, we notice that all the mixing energies exhibit linear trends, i.e., in the studied range of doping there are no visible cooperative effects. Secondly, we point out that Zn (pink) and Sc (brown)
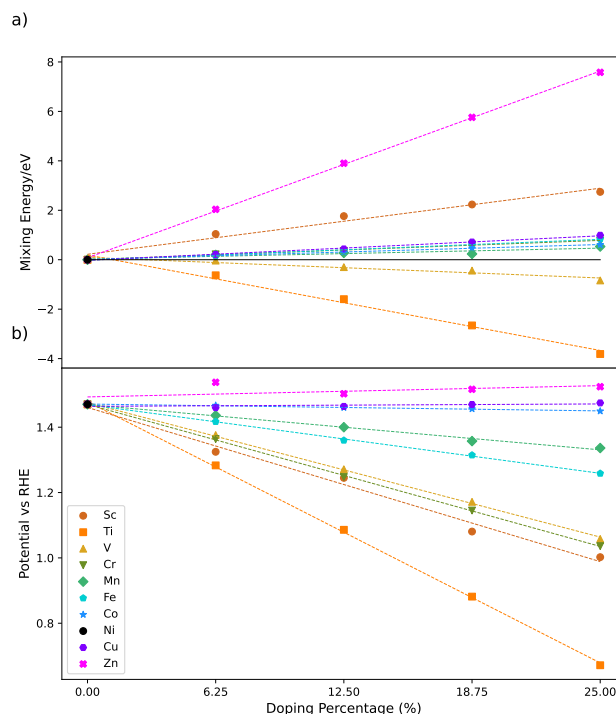

Figure 3: Influence of transition metal doping in NiOOH: a) Energy of mixing according to Eq. 6 depending on the percentage of transition metal in the bulk; b) Evolution of the Red/Ox potential of Eq. 8 depending on the percentage of transition metal in the bulk. The black point is for pure nickel (oxy)hydroxides.

offer the least favourable mixing. Zn is redox inactive and, thus, its incorporation in NiOOH leads to a proportional oxidation of Ni^{III} to Ni^{IV}, offering an explanation for the observed endothermic mixing energy. For Sc the reason is likely to be connected to its larger ionic size. Furthermore, ScOOH does not adopt a layered crystal structure, further indicating that its incorporation in $\beta-$NiOOH is unlikely achievable. Third, at the other extreme compared to Zn, we find Ti (orange) for which the mixing energy is very negative. However, this result is somewhat artificial, in the sense that in this case Ni^{III} is reduced to Ni^{II} to allow the formation of Ti^{IV}, the preferred oxidation state of Ti. In the oxyhydroxide, we also observe an internal electron transfer from V to Ni, so that Ni^{II} and V^{IV} co-exist in this case. Finally, we turn to the metals where doping is relevant according to the mixing energy: doping with Cu (purple), Co (dark blue), Fe (light blue), Mn (light green) and Cr (dark green) induces a slight increase in the mixing energy, which suggests that limited doping may be feasible, while at higher dopant concentrations we would expect a phase separation. In contrast, V (yellow) doping leads to a reduction in the mixing energy by almost 1 eV at 25% doping, which makes it a credibly achievable material. As shown in Fig. S2, the mixing energy in the Ni(OH)$_2$ phase is similar to the NiOOH phase, so that the most relevant dopants (Cr, Mn, Fe and Co) have a similar stability in both phases.

Having studied the stability of the investigated materials, we now turn to their redox potentials:

$$H^+ + e^- + (M_d^{III}, Ni_{1-d}^{III})OOH \rightarrow (M_d^{II}, Ni_{1-d}^{II})(OH)_2 \quad (8)$$

where d indicates the molar fraction of dopant M between 0.0625 to 0.25. As indicated in Eq. 8, all transition metals (M and Ni) are assumed to change their oxidation state from the +III oxidation state to +II. In practice, however, the oxidation state of the transition metals can vary depending on the specific dopant, with Ni compensating for these variations. For example, Zn will, of course, always stay in the +II state, so that some Ni atoms will need to adopt the +IV state, leading to $(Zn_d^{II}, Ni_d^{IV}, Ni_{1-2d}^{III})OOH$. The numerical results are presented in Figure 3b, where the evolution of the redox potential is shown as a function of the dopant percentage in the bulk structure. Like for the mixing energy, a nearly perfect linear behavior is observed for all dopants.

Doping with Zn (pink), Cu (purple), and Co (dark blue) slightly increases the redox potential of the bulk structures. Therefore, these dopants are of no interest for lowering the redox potential of the anode catalyst. Still, we remind the reader that we consider substitutional doping. In other words, our current results do not address the possibility of inducing bifunctionality or morphological changes. The other transition metals lower the redox potential of the bulk, which can be grouped into three categories: Mn (light green) and Fe (light blue) lower slightly the redox potential by 0.1-0.2 V; V (yellow) and Cr (dark green) reduce it by 0.3-0.4 V and Sc (brown) and Ti (orange) show a strong decrease of 0.4-0.8 V (for 25% dopant concentration). Given that the +II oxidation state of Sc and Ti are largely unknown, this strong decrease observed with Sc and Ti doping is due to the somewhat artificial $(M_d^{II}, Ni_{1-d}^{II})(OH)_2$ structure. As a consequence, Ti ans Sc are of no practical interest in this context. It is nevertheless worthwhile highlighting that Zn and Cu, for which the equivalent could have been said for the +III oxidation state, do not induce the opposite behavior. This is explained by the redox property of Ni: as seen in the bulk study, Ni^{IV} can be stabilized in the crystal structure by hydrogen bonds (see polymorph **E** in Fig. 1). In contrast, it is difficult to conceive Ni^I (necessary for, $(M_d^{III}, Ni_d^I, Ni_{1-2d}^{II})(OH)_2$).

The combined results of the influence of the dopants on the mixing energy and redox potential leads to the selection of a smaller subset of transition metals for further study. The mixing energy increases too significantly to allow for the stable formation of doped structures with Zn and Sc; similarly, Ti is eliminated from the selection due to the artificial $M_d Ni_{1-d}(OH)_2$ structure. Furthermore, given their negligible impact on the redox potential even at 25% doping concentration, we do not further study Co and Cu. Therefore, we investigate the surface properties only for Fe, Mn, Cr, and V doping and, to investigate the maximum effect, we focus on 25% doping.
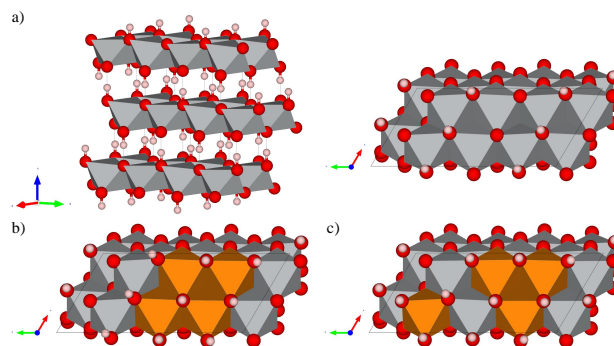

Figure 4: β-NiOOH optimized structure with 50% (a) side and top view, (b) 75% and (c) 87% H coverage. The Ni^{II} and Ni^{III} atoms are displayed in orange and gray, respectively. The vectors a, b and c are shown in red, green and blue, respectively.

3.3. NiOOH surface state from GC-DFT

Following our analysis of the oxidation behavior in the bulk, we now shift our focus to the redox properties at the surface. Before turning to the doped catalysts, we determine the pure NiOOH surface. While the catalytic activity is generally hypothesized to require a phase transition from $Ni(OH)_2$ to NiOOH, it is experimentally challenging to maintain a metastable NiOOH surface at potentials much lower than its bulk formation potential. Our surface models are thus derived based on a preconditioned NiOOH bulk, stabilized above 1.6 V vs RHE based on which we explore the surface state.

We have chosen a p(2 × 4) unit cell to represent the surface and explored hydrogen atom coverages ranging from 0% to 100% H coverage. This is achieved by adding or removing up to 4 hydrogen atoms starting from the stoichiometric NiOOH(50%) surface. Table 1 summarizes the oxidation states of the 8 nickel atoms in the surface layer as a function of hydrogen coverage at the potential of zero charge. We note that the fractionally charged surfaces used for GC-DFT at 1.5 V vs RHE closely follow these distributions of oxidation states, i.e., the fractional surface charge is spread out across several atoms. To better understand the relation between local Ni coordination and
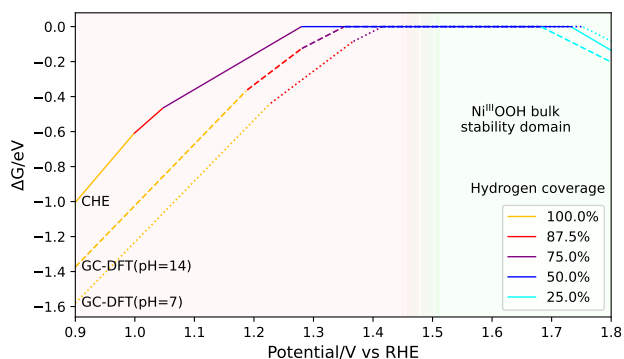

Figure 5: Most stable NiOOH surface hydrogen coverage as a function of electrochemical potential at pH 7 and 14.

Table 1
Percentages of Ni atoms in the upper layer of NiOOH surface by oxidation state for different hydrogen coverages. The numbers refer to the distribution at the potential of zero charge, but vary marginally at applied potentials.

H cov.	0%	12%	25%	37%	50%	62%	75%	87%	100%
Ni^{II}(%)	0	0	0	0	0	12.5	50	50	100
Ni^{III}(%)	50	62.5	75	87.5	100	87.5	50	50	0
Ni^{IV}(%)	50	37.5	25	12.5	0	0	0	0	0

oxidation state, Figure 4 depicts typical NiOOH surfaces, in particular the stoichiometric (50%) surface and partially reduced surfaces (75%, and 87% H coverage). Since we only add hydrogen atoms on the surface (not in the subsurface, where there is no space to accommodate them), even at 100% H coverage (i.e., adding four hydrogen atoms for eight surface Ni atoms), only 50% of the top layer nickel atoms should be in the Ni^{II} spin-state based on the stoichiometry. Still, 100% surface Ni^{II} are obtained, demonstrating that already five OH ligands (instead of six as in $Ni(OH)_2$) are enough to stabilize Ni^{II} centers. In agreement with the vanishing gap for all our surfaces, this higher-than-expected spin state is compensated by electrons that are delocalized over several Ni atoms. In the opposite direction (when the surface is oxidized), the percentage of Ni^{IV} strictly follows the number of hydrogen atoms that have been removed.

Figure 5 shows the most stable H coverage on the NiOOH surface as a function of the electrochemical potential, with the stoichiometric NiOOH(50%) structure as a reference for the relative energies. The bulk NiOOH stability domain is highlighted in light green and starts at about 1.5 V vs RHE. Results relying on the computational hydrogen electrode (CHE) are shown in full lines, while results that explicitly account for the electrochemical potential (and, thus, allow to distinguish between deprotonations and oxidations, see [55] for an example) via grand-canonical density functional theory (GC-DFT) are shown in dashed and dotted lines for pH 14 and 7, respectively. According to section S3 and Figure S4 the addition of a proton to the surface only leads to an increase in the surface charge of about 0.15 elementary charge at pH 14 and 1.5 V vs RHE. In other words, the proton and electron transfer are pretty much coupled and GC-DFT confirms that it is most relevant to talk about "hydrogenation" or "reduction" of the surface, not protonation. Additionally, the GC-DFT results are consistent with expectations as a function of the pH: at a given potential the H coverage either remains constant or decreases from pH 7 to pH 14. This highlights the advantage of using GC-DFT and justifies that we only discuss results at pH 14 in the following.

The stability diagram indicates that at pH 14 the most stable hydrogen coverage corresponds to 50% across the domain of potentials of interest, i.e., at potentials where NiOOH is stable ($\geq$ 1.47 V) and OER overpotentials are lower than 0.5 V ($\leq$ 1.73 V). The comparison with pH 7 indicates that in the case of a local drop of pH (due to the

faster consumption of OH$^-$ than what is replenished via diffusion) the surface might be covered with slightly more hydrogen atoms (75%), which already induces a partial reduction of Ni^{III} to Ni^{II} as discussed above. Figure S3 illustrates the relative stability of various hydrogen coverages on pure NiOOH at 1.4 V, 1.5 V, and 1.6 V vs RHE. Under operating conditions (1.5 V), reduction to the +II oxidation state is accessible with an energy cost of only 0.2 eV, which enables "chemical" oxidation of molecules via hydrogen atom transfers to the surface. At a lower potential (1.4 V), structures with hydrogen coverages ranging from 50% to 87% exhibit similar stabilities. In contrast, at a higher potential (1.6 V), the 50% hydrogen coverage remains the most stable configuration, but the formation to the +II oxidation state (62% H) becomes more difficult and is competitive with the formation of the +IV oxidation state (37% H), both being higher by +0.3 eV compared to the reference surface. Overall, it is remarkable that surface Ni^{IV} is formed at about 1.7 V vs RHE, a potential where NiO_2 is not yet the stable bulk (>1.9 V). In other words, on preconditioned NiOOH, Ni^{III} oxidation is facilitated, while reduction is inhibited compared to the bulk.

In summary, GC-DFT predicts that at pH 14 NiOOH mostly exposes the stoichiometric NiOOH surface: more reduced surfaces are only stable in a potential range where NiOOH itself is meta-stable and more oxidized surfaces become relevant at relatively high potentials, implying high ($\geq$ 0.5 V) overpotentials for the oxygen evolution reaction. Furthermore, the proton transfer reactions are tightly coupled with an electron transfer, suggesting that (de-)protonation reactions play a minor role for NiOOH. At the potential where NiOOH is stable our computations demonstrate that (i) hydrogen atom transfer mechanisms reducing Ni^{III} to Ni^{II}, as proposed by the classical Fleischmann mechanism, are credible at low potentials, but that the formation of Ni^{IV} is competitive at slightly higher potentials which might change the reactivity of the surface.

3.4. Modifications of the surface state via substitutional doping

From our study of the doping in the bulk, we decided to focus on V, Cr, Mn, and Fe to investigate the impact of these dopants on the surface state of doped NiOOH. In particular, given that these dopants lower the redox potential to reach the oxyhydroxide, we investigate if the surface oxidation also becomes more accessible compared to pure NiOOH. As seen in the previous section, NiOOH exposes a stoichiometric surface around the transition potential and requires potential > 1.7 V vs RHE for surface oxidation. If we focus on the hydrogen coverage of the doped surfaces at 1.3 V vs RHE, which is close to the phase-transition for the doped bulk materials, we can observe that the most stable hydrogen coverage is always higher (or equal, in the case of V) to the one obtained for pure NiOOH (Fig. S5 to Fig. S11). This increased hydrogen coverage upon doping, which goes along with a lower number of Ni^{III} sites, contrasts with the bulk redox potential, which was found to

be lowered by the introduction of a second metal. However, like for NiOOH, our GC-DFT computations do not evidence any significant (de-)protonation steps for these surfaces.
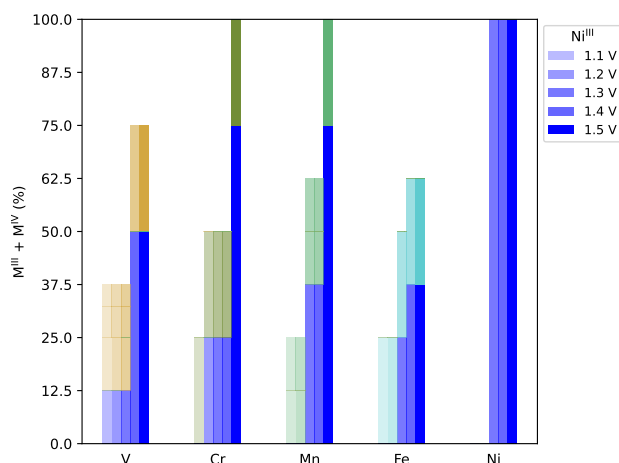

Figure 6: Percentage of Ni^{III} in blue and M^{III} (in a distinctive color) on the upper layer of NiOOH and $M_{0.25}Ni_{0.75}OOH$ surface depending on the applied potential (indicated by the shades) and the nature of the transition metal dopants. The presence of M^{IV}, distinguished by dashes, is compensated by additional Ni^{II} in the subsurface.

The number of Ni^{III} as a function of the dopant (V, Cr, Mn, or Fe) at 25% and of the applied potential are reported in Figure 6. As expected, at 1.5 V vs RHE, all Ni atoms are in the Ni^{III} state for the pure compound. Doping trivially reduces the overall number of nickel atoms present at the surface to a maximum of 75%. Moreover, our computations demonstrate that the proportion of Ni^{III} is always reduced, i.e., we never reach 75%, even at 1.5 V, except with 25% Cr. As a result, the number of active Ni^{III} sites available for electro-oxidation is generally diminished, potentially lowering the catalytic efficiency at 1.5 V vs RHE. The bulk redox potential of $Ni_{0.75}Fe_{0.25}OOH$ is about 1.3 V vs RHE, making the bulk stable at this potential, instead of metastable for pure NiOOH. Still, at the surface half of the metal ions are reduced, both at 1.3 and at 1.5 V vs RHE. This indicates that Fe doping results in a loss of surface active sites at all relevant potentials. The case of manganese doping is similar: the Ni^{III} species disappear below 1.3 V, which matches the calculated redox potential of the bulk Mn-doped NiOOH. Still, 12% of Mn^{III} and of Mn^{IV} are observed through the entire range of potentials, suggesting that Mn-doped NiOOH could be active at lower potentials than pure NiOOH provided that Mn can act as an active site. In contrast, in chromium and vanadium doped NiOOH, Ni^{III} species do remain present down to 1.1 V vs RHE. This indicates a unique stabilization of Ni^{III} in the presence of chromium and vanadium. Observing that all the chromium atoms remain in the +III oxidation state makes the case of chromium-doping all the more remarkable. V doping preferentially introduces V^{IV}, but the total number of oxidized sites remains > 30% across the probed range of potentials. The number of oxidized sites is reduced compared to pure NiOOH surface at 1.5 V but 12% of oxidized sites, equally shared between Ni^{III} and V^{IV}, are maintained even at 1.1 V vs RHE.

Our results highlight the complexity of assessing the impact of doping on the properties of NiOOH: From the bulk redox potential one would have expected a greater stability of Ni^{III} at lower potentials, while the surface hydrogen coverage indicates a more reduced surface compared to pure NiOOH. Finally, analysing the individual oxidation states suggest that Cr is the exception that partially corresponds to expectations: the hydrogen coverage on $Ni_{0.75}Cr_{0.25}OOH$ is equal or higher compared to pure NiOOH, but still allows for 25% of Ni^{III}, in addition to 25% Cr^{III}. Hence, in agreement with the lower bulk redox potential, Cr-doped NiOOH exposes active sites at lower potentials compared to pure NiOOH.

4. Conclusions

The bulk structure of β−NiOOH was found to have three proton arrangements that are highly competitive in relative energies. Only one of these proton ordering gives rise to stoichiometric slabs exposing the basal plane without creating a dipole moment. Therefore, this bulk is considered the most suitable for the investigation of the surface properties. Our computations have determined the redox potential from $Ni(OH)_2$ to NiOOH at 1.5 V vs. RHE, in quantitative agreement with experimental values, suggesting a reliable computational approach. Mixed Ni^{II}/Ni^{III} bulk structures have not been found to be stable at any potential, indicating that the phase-transition is thermodynamically abrupt with no intermediates. The predicted transition from NiOOH to NiO_2 is found to occur at 1.9 V, well beyond the range of potentials of interest.

For practical applications, a phase-transition at lower potentials is expected to reduce the overpotential for oxidation reactions. To identify a material with a lower redox potential, we investigated the effect of substitutional doping with up to 25% foreign metal. Our analysis includes two criteria: the stability, measured by the mixing energy (is the dopant more stable in the nickel matrix or in its own oxyhydroxide?) and the property of interest, i.e., the redox potential. Based on these factors, we identified V, Cr, Mn, and Fe as most promising, since they exhibited either negative or only slightly positive mixing energies and a significantly lower redox potential compared to pure Ni oxides.

Next, we studied the surface state of the β-NiOOH(0001) surface, focusing on the hydrogen coverage as a function of the electrochemical potential. We quantified the number of Ni^{II}, Ni^{III}, and Ni^{IV} species at the surface as a proxy for the number of active sites, which are generally assumed to be Ni^{III} around the onset potentials. Under working conditions for oxidation (around 1.5 V vs RHE), we found that 50% hydrogen coverage, corresponding to the stoichiometric NiOOH surface, is most stable and results in 100% of Ni^{III}

on the surface. Furthermore, our results demonstrate that dopants generally reduce the number of Ni^{III} active sites compared to pure NiOOH. Still, M^{III} species were also observed, which could act as active sites. Furthermore, Mn and Fe were shown to maintain Ni^{III} and M^{III} down to 1.3 V vs. RHE, which make them promising candidates. Cr maintains Ni^{III} even down to 1.2 V vs RHE, which is roughly the potential of the phase transition from the hydroxide to oxo-hydroxide phase. Further investigations should address the activity of such doped materials to actually catalyse oxidation reactions at lower potentials compared to pure NiOOH.

Acknowledgements

Data availability

The DFT raw data can be found under `doi.org/10.5281/zenodo.14205524` and visualized on nomad-lab.eu, `https://nomad-lab.eu/prod/v1/gui/user/datasets/dataset/id/f82s0e4zSyW2a9aq8nvr4Q`.

CRediT authorship contribution statement

Laureline Treps: Investigation, Writing - Original Draft. **Tony Ermacora:** Investigation, Writing - Original Draft. **Andrea Giacomelli:** Investigation. **Carine Michel:** Writing - Review & Editing. **Stephan N. Steinmann:** Supervision, Conceptualization, Writing - Review & Editing, Funding acquisition.

Bibliography

[1] Nathan S. Lewis and Daniel G. Nocera. Powering the planet: Chemical challenges in solar energy utilization. *Proceedings of the National Academy of Sciences*, 103(43):15729, 2006. doi: 10.1073/pnas.0603395103.

[2] Michael G. Walter, Emily L. Warren, James R. McKone, Shannon W. Boettcher, Qixi Mi, Elizabeth A. Santori, and Nathan S. Lewis. Solar water splitting cells. *Chem. Rev.*, 110(11):6446–6473, 2010. doi: 10.1021/cr1002326.

[3] Isolda Roger, Michael A. Shipman, and Mark D. Symes. Earth-abundant catalysts for electrochemical and photoelectrochemical water splitting. *Nat Rev Chem*, 1(1):1–13, 2017. doi: 10.1038/s41570-016-0003.

[4] Stephanie Nitopi, Erlend Bertheussen, Soren B. Scott, Xinyan Liu, Albert K. Engstfeld, Sebastian Horch, Brian Seger, Ifan E. L. Stephens, Karen Chan, Christopher Hahn, Jens K. Nørskov, Thomas F. Jaramillo, and Ib Chorkendorff. Progress and perspectives of electrochemical CO2 reduction on copper in aqueous electrolyte. *Chem. Rev.*, 119(12):7610–7672, 2019. doi: 10.1021/acs.chemrev.8b00705.

[5] P. W. T. Lu and S. Srinivasan. Electrochemical-ellipsometric studies of oxide film formed on nickel during oxygen evolution. *J. Electrochem. Soc.*, 125(9):1416, 1978. doi: 10.1149/1.2131689.

[6] J. K. Nørskov, J. Rossmeisl, A. Logadottir, L. Lindqvist, J. R. Kitchin, T. Bligaard, and H. Jónsson. Origin of the overpotential for oxygen reduction at a fuel-cell cathode. *J. Phys. Chem. B*, 108(46):17886–17892, 2004. doi: 10.1021/jp047349j.

[7] A. Van der Ven, D. Morgan, Y. S. Meng, and G. Ceder. Phase stability of nickel hydroxides and oxyhydroxides. *J. Electrochem. Soc.*, 153(2): A210, 2005. doi: 10.1149/1.2138572.

[8] F. Bardé, M. R. Palacín, B. Beaudoin, and J.-M. Tarascon. Ozonation: A unique route to prepare nickel oxyhydroxides. synthesis optimization and reaction mechanism study. *Chem. Mater.*, 17(3):470–476, 2005. doi: 10.1021/cm040133+.

[9] Fuding Lin and Shannon W. Boettcher. Adaptive semiconductor/electrocatalyst junctions in water-splitting photoanodes. *Nat. Mater.*, 13(1):81–86, 2014. doi: 10.1038/nmat3811.

[10] Minrui Gao, Wenchao Sheng, Zhongbin Zhuang, Qianrong Fang, Shuang Gu, Jun Jiang, and Yushan Yan. Efficient water oxidation using nanostructured α-nickel-hydroxide as an electrocatalyst. *J. Am. Chem. Soc.*, 136(19):7077–7084, 2014. ISSN 0002-7863. doi: 10.1021/ja502128j.

[11] Ming Gong and Hongjie Dai. A mini review of NiFe-based materials as highly active oxygen evolution reaction electrocatalysts. *Nano Res.*, 8(1):23–39, 2015. doi: 10.1007/s12274-014-0591-z.

[12] Ju Hao, Kaili Wu, Chaojie Lyu, Yuquan Yang, Hongjing Wu, Jiajia Liu, Naiyan Liu, Woon-Ming Lau, and Jinlong Zheng. Recent advances in interface engineering of fe/co/ni-based heterostructure electrocatalysts for water splitting. *Mater. Horiz.*, 10(7):2312–2342, 2023. doi: 10.1039/D3MH00366C.

[13] Michael Lyons and Michael Brandon. The oxygen evolution reaction on passive oxide covered transition metal electrodes in aqueous alkaline solution. part 1-nickel. *Int. J. Electrochem. Sci. International Journal*, 3(12):1386–1424, 2008. doi: 10.1016/S1452-3981(23)15531-3.

[14] Ye-Fei Li and Annabella Selloni. Mechanism and activity of water oxidation on selected surfaces of pure and Fe-doped NiOx. *ACS Catal.*, 4(4):1148–1153, 2014. doi: 10.1021/cs401245q.

[15] Vicky Fidelsky, Valeria Butera, Jeremie Zaffran, and Maytal Toroker. Three fundamental questions on one of our best water oxidation catalysts: a critical perspective. *Theor. Chem. Acc.*, 135(7):1432–2234, 2016. doi: 10.1007/s00214-016-1915-8.

[16] Alexander J. Tkalych, Kuang Yu, and Emily A. Carter. Structural and electronic features of β-Ni(OH)2 and β-NiOOH from first principles. *J. Phys. Chem. C*, 119(43):24315–24322, 2015. doi: 10.1021/acs.jpcc.5b08481.

[17] José C. Conesa. Electronic structure of the (undoped and Fe-doped) NiOOH o2 evolution electrocatalyst. *J. Phys. Chem. C*, 120(34): 18999–19010, 2016. doi: 10.1021/acs.jpcc.6b06100.

[18] Montse Casas-Cabanas, Maxwell D. Radin, Jongsik Kim, Clare P. Grey, Anton Van der Ven, and M. Rosa Palacín. The nickel battery positive electrode revisited: stability and structure of the β-NiOOH phase. *J. Mater. Chem. A*, 6(39):19256–19265, 2018. doi: 10.1039/C8TA07460G.

[19] M. Fleischmann, K. Korinek, and D. Pletcher. The oxidation of organic compounds at a nickel anode in alkaline solution. *Journal of Electroanalytical Chemistry and Interfacial Electrochemistry*, 31(1): 39–49, 1971. doi: 10.1016/S0022-0728(71)80040-2.

[20] M. Fleischmann, K. Korinek, and D. Pletcher. The kinetics and mechanism of the oxidation of amines and alcohols at oxide-covered nickel, silver, copper, and cobalt electrodes. *J. Chem. Soc., Perkin Trans. 2*, 2(10):1396–1403, 1972. doi: 10.1039/P29720001396.

[21] Michael T. Bender, Yan Choi Lam, Sharon Hammes-Schiffer, and Kyoung-Shin Choi. Unraveling two pathways for electrochemical alcohol and aldehyde oxidation on NiOOH. *J. Am. Chem. Soc.*, 142 (51):21538–21547, 2020. doi: 10.1021/jacs.0c10924.

[22] Lisa J. Enman, Michaela S. Burke, Adam S. Batchellor, and Shannon W. Boettcher. Effects of Intentionally Incorporated Metal Cations on the Oxygen Evolution Electrocatalytic Activity of Nickel (Oxy)hydroxide in Alkaline Media. *ACS Catal.*, 6(4):2416–2423, 2016. doi: 10.1021/acscatal.5b02924.

[23] Kun Zhao, Wenshu Yang, Longhua Li, Shuaishuai Wang, Ling Wang, Zhihao Qi, Yonggang Yang, Zhu Chen, Jinwei Zhuang, Jinhui Hao, and Weidong Shi. Discharge induced-activation of phosphorus-doped nickel oxyhydroxide for oxygen evolution reaction. *Chemical Engineering Journal*, 435:135049, 2022. doi: 10.1016/j.cej.2022.135049.

[24] Jiajun Wang, Lei Alexander Zhang, Yanmei Ren, and Ping Wang. Fluorine-doped nickel oxyhydroxide as a robust electrocatalyst for oxygen evolution reaction. *Electrochimica Acta*, 437:141475, 2023. doi: 10.1016/j.electacta.2022.141475.

[25] Sangeeta Adhikari, Stephan N. Steinmann, Maheswari Arunachalam, Soon Hyung Kang, and Do-Heyoung Kim. Unraveling the Oxidation Kinetics Through Electronic Structure Regulation of MnCo2O4.5@Ni3S2 p–n Junction for Urea-Assisted Electrocatalytic Activity. *Small*, 20(40):2311548, 2024. doi: 10.1002/smll.202311548.

[26] Hui Ding, Hongfei Liu, Wangsheng Chu, Changzheng Wu, and Yi Xie. Structural Transformation of Heterogeneous Materials for Electrocatalytic Oxygen Evolution Reaction. *Chem. Rev.*, 121(21): 13174–13212, 2021. doi: 10.1021/acs.chemrev.1c00234.

[27] Mikaela Görlin, Petko Chernev, Jorge Ferreira de Araújo, Tobias Reier, Sören Dresp, Benjamin Paul, Ralph Krähnert, Holger Dau, and Peter Strasser. Oxygen evolution reaction dynamics, faradaic charge efficiency, and the active metal redox states of ni–fe oxide water splitting electrocatalysts. *J. Am. Chem. Soc.*, 138(17):5603–5614, 2016. doi: 10.1021/jacs.6b00332.

[28] Fengli Yang, Mauricio Lopez Luna, Felix T. Haase, Daniel Escalera-López, Aram Yoon, Martina Rüscher, Clara Rettenmaier, Hyo Sang Jeon, Eduardo Ortega, Janis Timoshenko, Arno Bergmann, See Wee Chee, and Beatriz Roldan Cuenya. Spatially and Chemically Resolved Visualization of Fe Incorporation into NiO Octahedra during the Oxygen Evolution Reaction. *J. Am. Chem. Soc.*, 145(39):21465–21474, 2023. doi: 10.1021/jacs.3c07158.

[29] J. K. Nørskov, T. Bligaard, J. Rossmeisl, and C. H. Christensen. Towards the computational design of solid catalysts. *Nat. Chem.*, 1(1):37–46, 2009. doi: 10.1038/nchem.121.

[30] Peilin Liao, John A. Keith, and Emily A. Carter. Water oxidation on pure and doped hematite (0001) surfaces: Prediction of co and ni as effective dopants for electrocatalysis. *J. Am. Chem. Soc.*, 134(32): 13296–13309, 2012. doi: 10.1021/ja301567f.

[31] Rutger A. van Santen and Philippe Sautet. *Computational Methods in Catalysis and Materials Science: An Introduction for Scientists and Engineers | Wiley*. doi: 10.1002/9783527625482.

[32] Daniel Friebel, Mary W. Louie, Michal Bajdich, Kai E. Sanwald, Yun Cai, Anna M. Wise, Mu-Jeng Cheng, Dimosthenis Sokaras, Tsu-Chien Weng, Roberto Alonso-Mori, Ryan C. Davis, John R. Bargar, Jens K. Nørskov, Anders Nilsson, and Alexis T. Bell. Identification of highly active Fe sites in (Ni,Fe)OOH for electrocatalytic water splitting. *J. Am. Chem. Soc.*, 137(3):1305–1313, 2015. doi: 10.1021/ja511559d.

[33] Oscar Diaz-Morales, Isis Ledezma-Yanez, Marc T. M. Koper, and Federico Calle-Vallejo. Guidelines for the rational design of ni-based double hydroxide electrocatalysts for the oxygen evolution reaction. *ACS Catal.*, 5(9):5380–5387, 2015. doi: 10.1021/acscatal.5b01638.

[34] Nawras Abidi, Kang Rui Garrick Lim, Zhi Wei Seh, and Stephan N. Steinmann. Atomistic modeling of electrocatalysis: Are we there yet? *WIREs Comput. Mol. Sci.*, 11(3):e1499, 2021. doi: 10.1002/wcms.1499.

[35] Nawras Abidi, Audrey Bonduelle-Skrzypczak, and Stephan N. Steinmann. How to dope the basal plane of 2H-MoS2 to boost the hydrogen evolution reaction? *Electrochim. Acta*, 439:141653, 2023. doi: 10.1016/j.electacta.2022.141653.

[36] Antton Curutchet, Pauline Colinet, Carine Michel, Stephan N. Steinmann, and Tangui Le Bahers. Two-sites are better than one: revisiting the OER mechanism on CoOOH by DFT with electrode

[37] Christopher D. Taylor, Sally A. Wasileski, Jean-Sebastien Filhol, and Matthew Neurock. First principles reaction modeling of the electrochemical interface: Consideration and calculation of a tunable surface potential from atomic and electronic structure. *Phys. Rev. B*, 73(16):165402, 2006. doi: 10.1103/PhysRevB.73.165402.

[38] Ravishankar Sundararaman, William A. Goddard, III, and Tomas A. Arias. Grand canonical electronic density-functional theory: Algorithms and applications to electrochemistry. *The Journal of Chemical Physics*, 146(11):114104, 2017. doi: 10.1063/1.4978411.

[39] Haochen Zhang, William A. Goddard, Qi Lu, and Mu-Jeng Cheng. The importance of grand-canonical quantum mechanical methods to describe the effect of electrode potential on the stability of intermediates involved in both electrochemical CO2 reduction and hydrogen evolution. *Phys. Chem. Chem. Phys.*, 20(4):2549–2557, 2018. doi: 10.1039/C7CP08153G.

[40] Nicolas G. Hörmann, Oliviero Andreussi, and Nicola Marzari. Grand canonical simulations of electrochemical interfaces in implicit solvation models. *J. Chem. Phys.*, 150(4):041730, 2010. doi: 10.1063/1.5054580.

[41] Marko M. Melander, Mikael J. Kuisma, Thorbjørn Erik Køppen Christensen, and Karoliina Honkala. Grand-canonical approach to density functional theory of electrocatalytic systems: Thermodynamics of solid-liquid interfaces at constant ion and electrode potentials. *J. Chem. Phys.*, 150(4):041706, 2019. doi: 10.1063/1.5047829.

[42] G. Kresse and J. Furthmüller. Efficient iterative schemes for ab initio total-energy calculations using a plane-wave basis set. *Physical Review B*, 54(16):11169–11186, 1996. doi: 10.1103/PhysRevB.54.11169.

[43] P. E. Blöchl. Projector augmented-wave method. *Physical Review B*, 50(24):17953–17979, 1994. doi: 10.1103/PhysRevB.50.17953.

[44] John P. Perdew, Kieron Burke, and Matthias Ernzerhof. Generalized Gradient Approximation Made Simple. *Physical Review Letters*, 77 (18):3865–3868, 1996. doi: 10.1103/PhysRevLett.77.3865.

[45] Stephan N Steinmann and Clemence Corminboeuf. Comprehensive benchmarking of a density-dependent dispersion correction. *Journal of chemical theory and computation*, 7(11):3567–3577, 2011. doi: 10.1021/ct200602x.

[46] Ye-Fei Li and Zhi-Pan Liu. Structure and water oxidation activity of 3d metal oxides. *WIREs Computational Molecular Science*, 6(1):47–64, 2016. doi: 10.1002/wcms.1236.

[47] Kiran Mathew, V. S. Chaitanya Kolluru, Srinidhi Mula, Stephan N. Steinmann, and Richard G. Hennig. Implicit self-consistent electrolyte model in plane-wave density-functional theory. *The Journal of Chemical Physics*, 151(23):234101, 2019. doi: 10.1063/1.5132354.

[48] Vei Wang, Nan Xu, Jin-Cheng Liu, Gang Tang, and Wen-Tong Geng. Vaspkit: A user-friendly interface facilitating high-throughput computing and analysis using vasp code. *Computer Physics Communications*, 267:108033, 2021. doi: https://10.1016/j.cpc.2021.108033.

[49] Mohammad Javad Eslamibidgoli, Axel Groß, and Michael Eikerling. Surface configuration and wettability of nickel(oxy)hydroxides: a first-principles investigation. *Phys. Chem. Chem. Phys.*, 19(34): 22659–22669, 2017. doi: 10.1039/C7CP03396F.

[50] Jeremie Zaffran and Maytal Caspary Toroker. Benchmarking Density Functional Theory Based Methods To Model NiOOH Material Properties: Hubbard and van der Waals Corrections vs Hybrid Functionals. *Journal of Chemical Theory and Computation*, 12(8):3807–3812, 2016. doi: 10.1021/acs.jctc.6b00657.

[51] Michael K. Carpenter and Dennis A. Corrigan. Photoelectrochemistry of nickel hydroxide thin films. *J. Electrochem. Soc.*, 136(4):1022, 1989. doi: 10.1149/1.2096777.

[52] Michael J. Natan, Daniel. Belanger, Michael K. Carpenter, and Mark S. Wrighton. pH-sensitive nickel(II) hydroxide-based microelectrochemical transistors. *J. Phys. Chem.*, 91(7):1834–1842, 1987. doi: 10.1021/j100291a031.

[53] G. Barral, F. Njanjo-Eyoke, and S. Maximovitch. Characterisation of the passive layer and of hydroxide deposits of nickel by impedance

spectroscopy. *Electrochimica Acta*, 40(17):2815–2828, 1995. doi: 10.1016/0013-4686(95)00274-I.

[54] Prashanth W. Menezes, Shenglai Yao, Rodrigo Beltrán-Suito, J. Niklas Hausmann, Pramod V. Menezes, and Matthias Driess. Facile access to an active γ-NiOOH electrocatalyst for durable water oxidation derived from an intermetallic nickel germanide precursor. *Angewandte Chemie International Edition*, 60(9):4640–4647, 2021. doi: 10.1002/anie.202014331.

[55] Nawras Abidi, Amit Sahu, Pascal Raybaud, and Stephan N. Steinmann. Electrochemical Potential-Dependent Stability and Activity of MoS3 during the Hydrogen Evolution Reaction. *ACS Catal.*, 13 (23):15290–15300, 2023. doi: 10.1021/acscatal.3c03292.